SKS Polarization Anomalies Due to the Coriolis Force

Neala Creasy[*1,2], Ebru Bozdağ[2,3], Daniel A. Frost[4], and Roel Snieder[2]

ABSTRACT

The Earth's Coriolis force has been well-known to impact surface waves and normal modes, which is essential to accurately interpret these waves. However, the Coriolis force on body waves has been assumed to be negligible and mostly ignored. It has been previously shown that the Coriolis force impacts polarizations of shear waves, whereas the wavefronts remain unaffected. We expand on the potential influences of Earth's Coriolis force on shear-wave polarization measurements by conducting 3D numerical simulations for elastic waves generated by earthquake and explosive sources in a radially symmetric, and 3D mantle and crustal models. The Coriolis force can produce polarization anomalies of mantle shear waves up to 7° and core phases, such as *SKS* and *SKKS*, up to 4°. Uncorrected shear-wave polarizations due to the Coriolis force can cause an additional source of error (5°–10° in fast direction, and 0.2–0.3 s delay time depending on the method and seismic phase), inaccurate interpretation of station misalignments, and imprecise estimates of the core–mantle boundary topography. We show how to correct for the Coriolis force on teleseismic shear waves using 1D ray tracing for well-isolated phases. We recommend the use of full waveform simulations to accurately account for earthquake sources parameters, poorly isolated phases that could include interfering phase arrivals within the measurement time window, and the effect of the Coriolis force on the polarizations of shear waves.

KEY POINTS

- The Coriolis force influences polarizations of shear waves.
- Coriolis force affects interpretations of Earth's structure that rely on accurate polarization measurements.
- We offer a remedy to correct polarization measurements using 1D ray tracing or seismic numerical modeling.

Supplemental Material

INTRODUCTION

Significant contributions in seismology have proven the impact of the Coriolis force on normal modes (Backus and Gilbert, 1961; Dahlen and Tromp, 1998) and surface waves (e.g., Tromp, 1994; Park and Gilbert, 1986; Snieder and Sens-Schönfelder, 2021). However, the influence of Coriolis force on body waves has been considered negligible, as Schoenberg and Censor (1973) illustrated the effect of rotation on body waves within an elastic, isotropic, and rotating homogeneous medium, showing that Earth's rotation can cause a dispersive and transversely isotropic effect. Using the plane-wave solution to the wave equation, body waves are virtually not affected when the travel time of the body wave is much less than the rotational period of the Earth (a day). Snieder *et al.* (2016) also showed that the polarization of shear wave propagating through the Earth is deviated over a few degrees by Earth's rotation, and that the Coriolis force minimally affects *P*-wave polarizations but leads to the slow rotation of the *S*-wave's transverse polarization (like a Foucault pendulum). The resulting polarization deviates from the expected polarization, which can be determined by the source mechanism and any reflections or transmissions that may occur along the *S*-wave's ray path.

As a result, polarization anomalies due to the Coriolis force may influence seismological measurements that rely on shear-wave polarization. Snieder *et al.* (2016) hypothesized that Earth's Coriolis force could also impact *SKS* shear-wave splitting (SWS) measurements (e.g., fast-axis polarization, delay time, and splitting intensity) by causing *SKS* polarizations to rotate out of the great circle plane. SWS is the measure of

1. Earth and Environmental Sciences Division, Los Alamos National Lab, Los Alamos, New Mexico, U.S.A., https://orcid.org/0000-0002-2557-6247 (NC); 2. Department of Geophysics, Colorado School of Mines, Golden, Colorado, U.S.A., https://orcid.org/0000-0003-1445-0857 (RS); 3. Department of Applied Mathematics and Statistics, Colorado School of Mines, Golden, Colorado, U.S.A.; 4. School of the Earth, Ocean, and the Environment College of Arts and Sciences, University of South Carolina, Columbia, South Carolina, U.S.A., https://orcid.org/0000-0001-7882-5166 (DAF)

*Corresponding author: nmcreasy@lanl.gov

Cite this article as Creasy, N., E. Bozdağ, D. A. Frost, and R. Snieder (2023). *SKS* Polarization Anomalies Due to the Coriolis Force, *Bull. Seismol. Soc. Am.* **XX**, 1–14, doi: 10.1785/0120230125

travel-time differences between orthogonal, polarized wavelets, and commonly describes seismic anisotropy, as caused by crystal-preferred orientation of minerals within the Earth's mantle and crust (Silver and Chan, 1991; Savage, 1999). In SWS studies, differences between the initial polarization direction and great-circle back azimuth are commonly observed (e.g., Restivo and Helffrich, 2006; Walpole *et al.*, 2014). These polarization deviations will lead to inaccurate SWS measurements based on the degree of the polarization deviation and the SWS method (Tian *et al.*, 2011). In a radially symmetric and nonrotating Earth, the *SKS* polarization should be aligned with the great-circle back azimuth (the orientation of the earthquake-receiver plane) due to the *P*-to-*SV* conversion at the core–mantle boundary (CMB). Observed polarization deviations for *SKS* and *SKKS* from the great-circle back azimuth have been attributed to isotropic heterogeneities, velocity gradients, scattering, topography, and/or misalignment of seismographs (e.g., Restivo and Helffrich, 2006; Reiss and Rümpker, 2017; Eakin *et al.*, 2018).

Therefore, in this study, we investigate the impact of the Coriolis force on the polarization of shear waves, including *SKS*, with 3D global wave simulations. We use the open-source 3D global wave propagation solver, SPECFEM3D GLOBE (Komatitsch and Tromp, 2002a,b), to simulate waves excited by explosive and earthquake sources, propagating in a rotating and nonrotating Earth to constrain the effect of rotation on a variety of teleseismic body waves. We simulate wave propagation for two types of Earth models: isotropic, radially symmetric (preliminary reference Earth model [PREM]: Dziewonski and Anderson, 1981), and 3D global mantle models (GLAD-M15 and GLAD-M25: Bozdağ *et al.*, 2016; Lei *et al.*, 2020), which can include 3D crustal variations. We demonstrate the effect of Earth's rotation on shear-wave polarizations, while also demonstrating that Earth's rotation does not impact back azimuthal projection measurements. Finally, we discuss the implications of Earth's rotation on certain types of measurements, such as SWS and polarization analysis.

NUMERICAL SIMULATIONS

We compute 30 min, global synthetic seismograms by the 3D spectral-element global wave propagation package SPECFEM3D GLOBE (Komatitsch and Tromp, 2002a,b). In the solver, the globe is divided into six chunks, for which we apply 480 spectral elements along one side of each chunk at the surface, resolving down to the minimum period of ~ 9 s. For the radially symmetric model, we use isotropic PREM (Dziewonski and Anderson, 1981) and include Earth's rotation, attenuation, ellipticity, gravity (Cowling approximation), and the ocean load (Komatitsch and Tromp, 2002a). We perform simulations for the 3D, heterogeneous mantle but also include surface topography and lateral crustal variations using model GLAD-M15 (Bozdağ *et al.*, 2016), because it has been established that crustal heterogeneities can significantly impact surface waves (Bozdağ and Trampert, 2008; Ferreira *et al.*, 2010; Lekic *et al.*, 2010) and body waves (Ritsema *et al.*, 2009). For selected events, we perform simulations for GLAD-M25 (Lei *et al.*, 2020), which is the successor of GLAD-M15 with higher resolution and stronger velocity perturbations. In addition, we use the same Earth models and simulation parameters for selected sources, but remove Earth's rotation from simulations to evaluate the Coriolis force. All synthetics are band-pass filtered between 10 and 50 s. We perform simulations with a variety of earthquake source types, including explosive sources, defined double-couple focal mechanisms, and realistic earthquakes to account for any source effects (receivers and 98 earthquakes used: Fig. 1).

RESULTS: EARTH'S CORIOLIS FORCE AND BODY-WAVE POLARIZATION MEASUREMENTS

Here, we present how the Earth's Coriolis force impacts body-wave polarizations for explosive and earthquake sources.

Explosive sources

To illustrate the direct impact of Earth's Coriolis force on shear-wave polarizations and avoid any source effects, we perform wave simulations with two explosive sources using PREM (Table S1, available in the supplemental material to this article), in which *S* waves are only generated by conversions at interfaces within the Earth. We place two identical explosive sources (M_w 6.0) along the prime meridian at a depth of 20 km at 60° N and 60° S; Fig. 2a, sources are offset to show direction of propagation). We use a global distribution of 1095 stations. Figure 2 illustrates the influence of the Coriolis force on *P*-to-*S* converted phases (e.g., *PKS*), which should all have particle motions aligned with great circle path back azimuth.

Figure 2b illustrates the effect of Earth's rotation on the polarization of *PKS* phases generated for these events, propagating in opposite directions. The radial component waveforms are identical, but the transverse components have opposite signs for the two sources due to the direction of propagation relative to the Earth's rotation axis. The *PKS* phase is selected as an example because the source is explosive in a 1D Earth, for which only *P*-wave energy is produced; therefore, *P*-to-*SV* conversions can be isolated to analyze the polarizations of shear waves. In addition, these phases are used for SWS. Based on Figure 2, waves propagating parallel to the Earth's rotation axis (due north) experience clockwise rotation of the polarizations. However, waves propagating anti-parallel to the Earth's rotation axis (due south) experience a counterclockwise rotation of the polarizations. In the nonrotating Earth example (Fig. 2), *PKS* is aligned with the great-circle back azimuth, resulting in negligible energy on the transverse component.

Any polarization anomaly is defined as the angle (in degrees) of the particle motion relative to the radial direction, which is along the great-circle back azimuth from receiver to

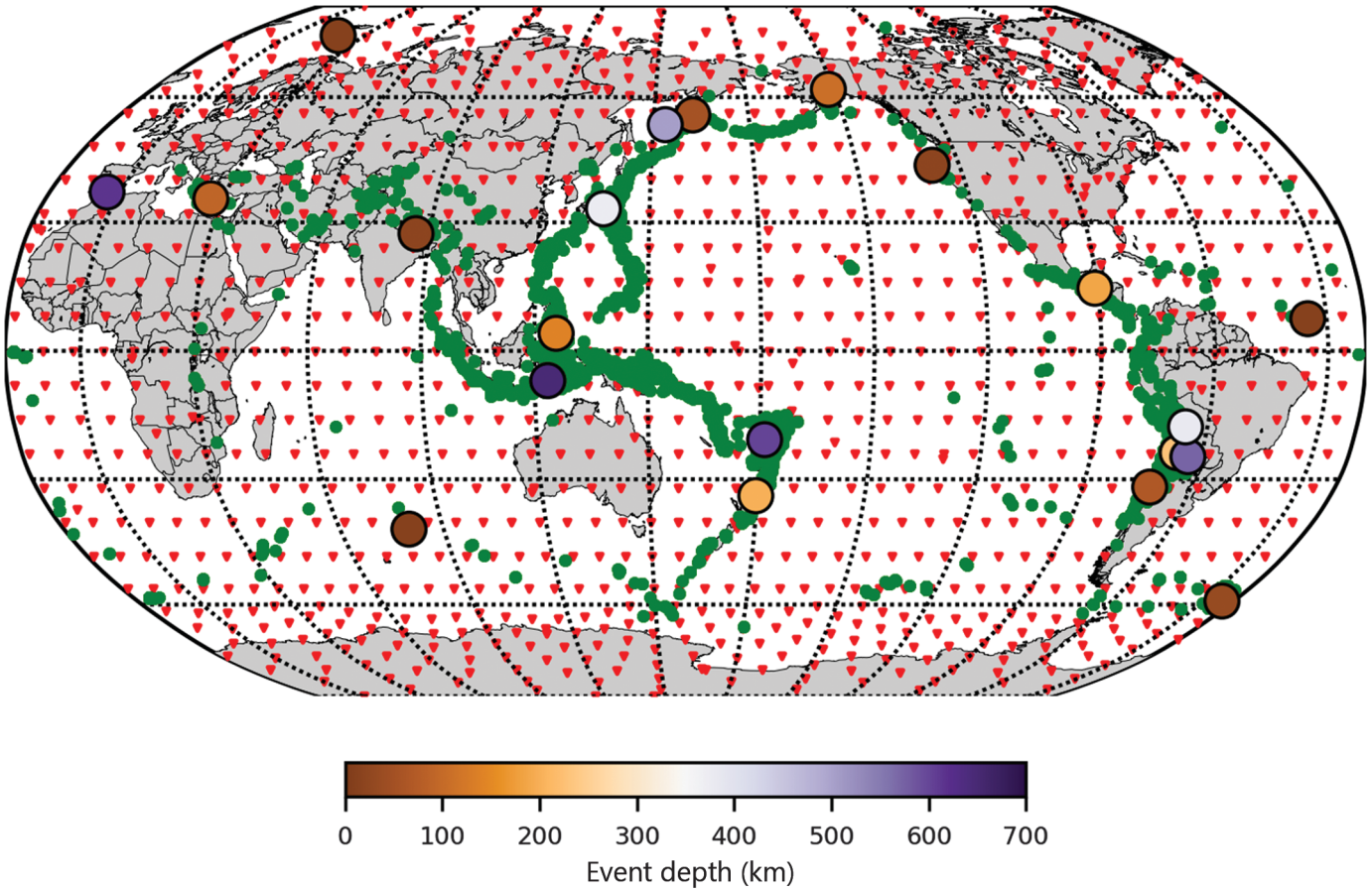

Figure 1. All pseudoreceivers (red triangles) and events (circles, colored by event depth in kilometers) used in this study. Green dots are event locations from the Walpole *et al.* (2014). These events are used for Figure 9.

source. To measure polarizations, we calculate a least-squares line fit to the particle motion by selecting a time window over the selected phase. Then, we calculate the angle of the particle motion relative to north.

We show measured polarizations of *P*, *pS*, *PS*, *PcS*, *pSKS*, and *PKS* phases for the two explosive sources (Fig. 3). Similar to Snieder *et al.* (2016), we detect no noticeable polarization deviations for the direct *P* (Fig. 3) and *PP* (Fig. 2b) phases. Mantle phases, *pS*, *PS*, and *PcS*, have polarization deviations of 2°–7°. Core phases, *pSKS* and *PKS*, only deviate 2°–3°. Polarization anomalies vary due to source location and propagation time, for which longer propagating phases result in larger polarization deviations. One interesting observation is that not all azimuths that propagate along the poles result in the largest polarization anomalies. The Coriolis force will switch the polarity of the polarization effect when a ray crosses a pole, which causes a decrease in the polarization anomaly with growing distance. This phenomenon is well demonstrated in Figure 3. For *pS* that crosses the southern pole (for the southern explosive event at an azimuth of 180°), there is no polarization anomaly; but the strongest anomaly exists because the ray does not cross the poles at all when *pS* propagates north (azimuth of 0°).

Realistic earthquake sources

To estimate the impact of Earth's Coriolis force for realistic earthquakes, we show simulations with our global pseudostation network and 21 earthquakes (Fig. 1, Table S2) selected from the Global Centroid Moment Tensor catalog (Ekström *et al.*, 2012) to observe the Coriolis force on other shear waves that are also relevant to SWS (i.e., *SKS*, *SKKS*, S_{diff}, *ScS*, S, etc.), because they are not strongly excited in the explosive simulations. Figure 4 illustrates the energy introduced to the *SKS*, *SKKS*, and S_{diff} transverse component due to Earth's Coriolis force in PREM for a selected deep event (M_w 6.3, 380 km depth, 2019 Central Bolivia event; see Table S2), for which this energy is absent for *SKS* and *SKKS* for a nonrotating, layered Earth. We select one earthquake from our entire simulation set to illustrate the impact for the Coriolis force. We measure all polarizations of *SKS* for a nonrotating and rotating Earth for this earthquake. Subtracting these two polarization measurements isolates the influence of the Coriolis force (Fig. 4d). Polarization anomalies vary from −2° to 1°, which exceed the error in polarization measurements from real data (~0.3° ± 0.2°, Walpole *et al.*, 2014). Large deviations in polarizations occur near the nodal planes of the radiation pattern, because the signal-to-noise ratio is lower along these azimuths.

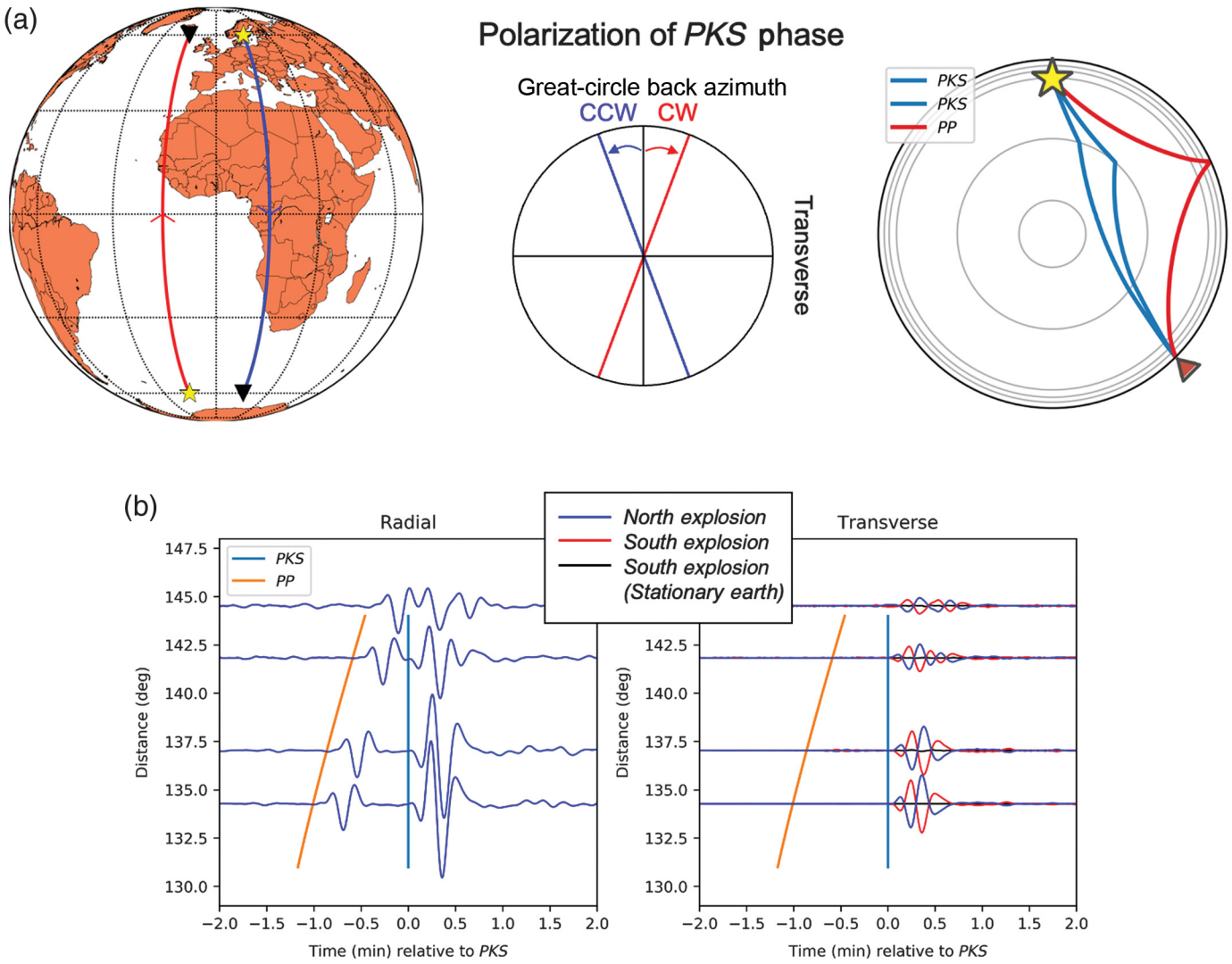

Figure 2. (a) *PKS* propagating north (event: yellow star, pseudoreceiver: black triangle) produces negative (red) polarization deviations from the back azimuth or rotating in the clockwise direction (CW). *PKS* propagating south is polarized positively (blue) or rotating in the counterclockwise (CCW) direction. The polarization deviations are exaggerated. Corresponding ray paths of *PKS* are shown propagating from an earthquake (yellow star) to a receiver (red triangle). (b) Radial and transverse component synthetics of *PP* (orange) and *PKS* (light blue) at opposite stations, plotted relative to the *PKS* arrival time. Transverse component is multiplied by 10 to visualize the effect of the Coriolis force. Synthetics of the northern explosion (blue), synthetics of southern explosion (red), and synthetics of the southern explosion for a nonrotating Earth (black).

Figure S1 shows the influence of the Coriolis force on *S* and *ScS* polarizations. To remove the source-radiation effect, we subtract the polarizations of the nonrotating Earth from the polarizations of the rotating Earth. The same pattern can be observed for *S* and *ScS* polarization anomalies, yet they vary from −6° to 3°, exceeding the anomalies measured for *SKS* and *PKS*. An *S* wave at 60° distance has a ∼18 min travel time, whereas the *SKS* phase has a total of 26 min travel time at 120°, which would intuitively lead to larger anomalies for *SKS* waves than for *PKS* waves. However, only the shear wave from the CMB to the receiver, which has a travel time of ∼8 min, is retained by the Coriolis force. Consequently, mantle shear waves are more impacted, since the Coriolis force will be retained along the whole direct *S* ray path. We also evaluate the effect of ellipticity, which can cause negligible polarization anomalies of $< |0.5|°$ (Fig. S11).

Idealized double-couple sources

The realistic earthquakes in the previous section all contain isotropic and calibrated linear vector dipole (CLVD) components. To effectively illustrate the influence of the source nodal planes on polarization measurements, we also conduct simulations for events that are purely double couple. The expected polarizations of the various core phases can deviate from the expected values, because the *SV* energy is negligible near the nodal planes. Therefore, we included some tests with perfect double-couple sources for a vertical dip-slip, strike slip, and oblique scenarios. The results are presented in Figure 5. In the nonrotating Earth, all propagation paths far from a nodal

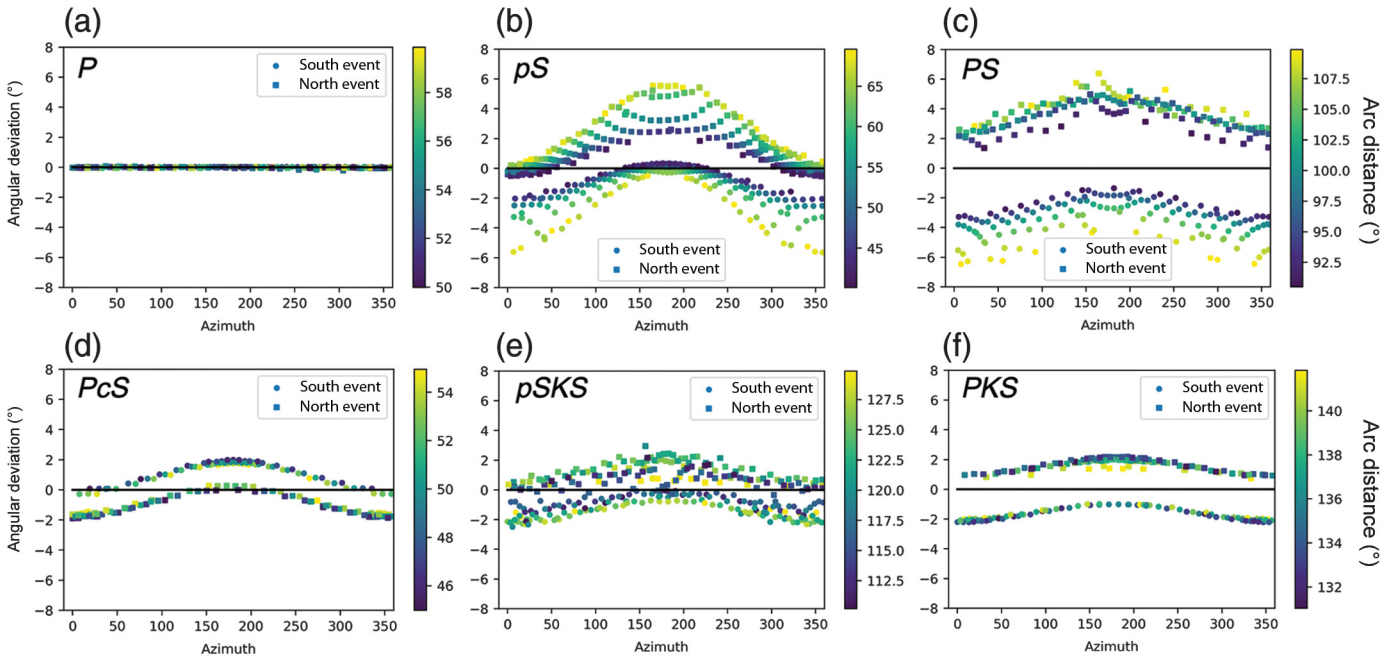

Figure 3. Illustrating measured polarizations from selected windows of each phase: (a) *P*, (b) *pS*, (c) *PS*, (d) *PcS*, (e) *pSKS*, and (f) *PKS* from the explosive events in Figure 2. Azimuth (in degrees) is the ray-path direction from the event. Two datasets are displayed, one from the event at 60° N (squares) and the other at 60° S (circles). Each dot is colored by arc distance (°).

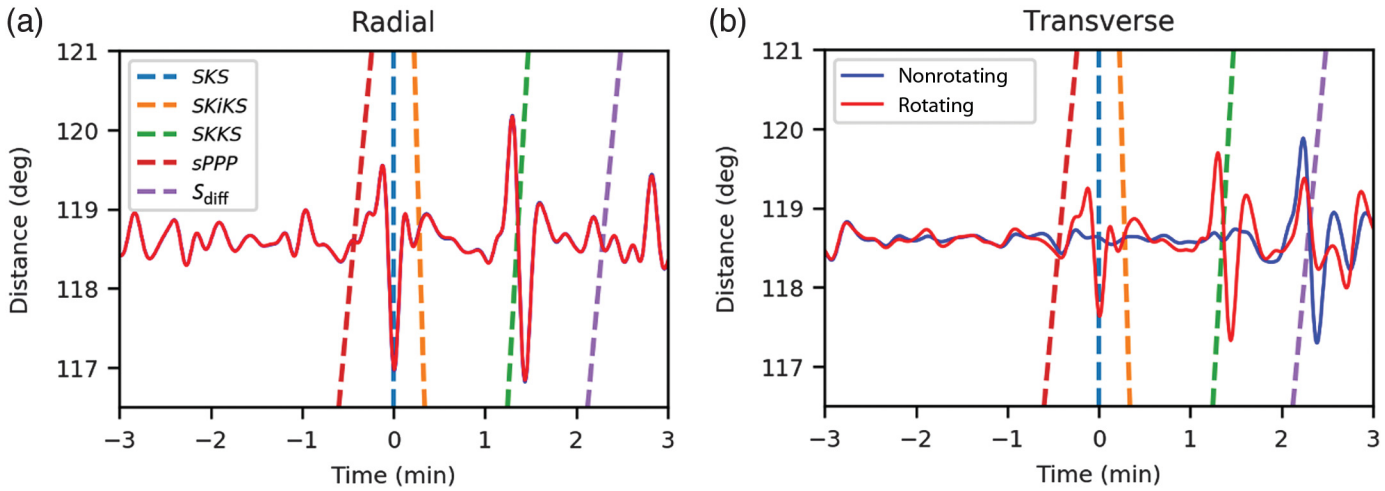

Figure 4. (a) Radial synthetics of preliminary reference Earth model (PREM; min) plotted relative to *SKS* (blue) at 119°. *SKKS* (green), *SKiKS* (yellow), *sPPP* (red), and S_{diff} (purple) arrival times shown with dashed lines. Synthetics modeled with PREM (blue [nonrotating Earth] and red [rotating Earth] lines). (b) Same as panel (a) but the transverse component, which is multiplied by 10 to visualize the effect of the Coriolis force.

plane show no angular deviation from the back azimuth; however, there are clear strong deviations when the azimuth from the event is near a nodal plane. When including Earth's rotation, those deviations due to the nodal planes are still present and are then overprinted on the Coriolis force. Therefore, polarization measurements are prone to errors (more than 10°) for waves radiated near a nodal plane.

Fitting polarizations with the Coriolis force

To correct *S*-wave polarization caused by the Coriolis force from the previous three sections, the rate of change in the shear-wave polarization can be easily calculated from the work of Snieder *et al.* (2016). Correcting for the Coriolis force will result in more accurate interpretations of polarizations for all *S* waves. The rate of polarization

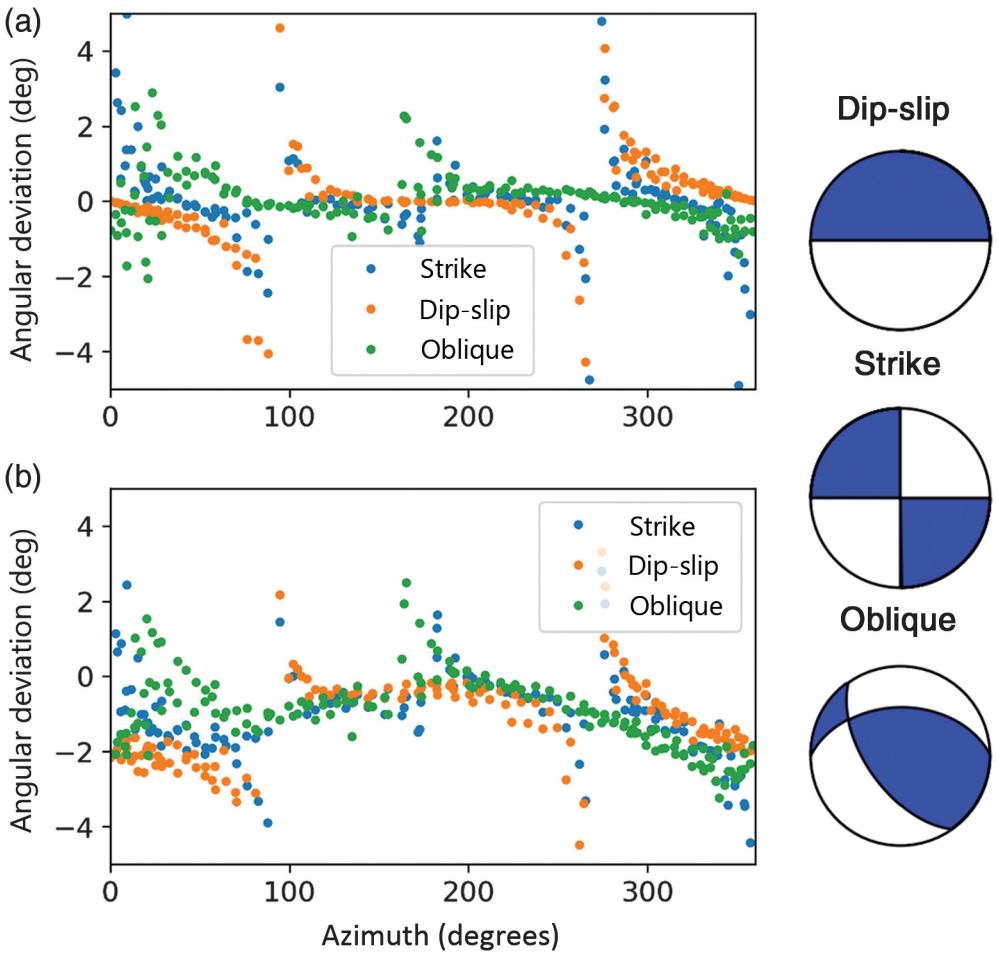

Figure 5. Polarization measurements (angular deviation, in degrees) for PREM of *SKS* for three different perfect double-couple sources located at 60° S plotted over azimuth from the source at a depth of 20 km. (a) Calculated synthetics for a nonrotating Earth and (b) for a rotating Earth (arc distances of 105°–140°). Focal mechanism plot diagrams of each source type represent vertical dip-slip, strike slip, and 45°-dipping oblique.

rotation is given by the following dot product (assuming high frequencies of body waves):

$$\dot{\phi} = -\vec{\Omega} \cdot \hat{u}, \tag{1}$$

in which ϕ is the polarization direction of a shear wave, Ω is the Earth's rotation vector, $\hat{u}$ is the ray direction, and the $\dot{\phi}$ denotes the time derivative, which can be simplified further to

$$\dot{\phi} = -\Omega \cos\theta. \tag{2}$$

In these expressions, Ω is the rotation rate of the Earth, and θ is the angle between the ray direction ($\hat{u}$) and Earth's rotation axis ($\vec{\Omega}$). Integrating this expression over the travel time along the ray gives the total polarization anomaly

$$\phi = -\int \Omega \cos\theta dt, \tag{3}$$

in which t is the travel time of the ray.

Polarization anomalies due to the Coriolis force can be calculated with ray tracing, which is applied to equation (3). We use 1D ray tracing with PREM, using the TauP software (Crotwell *et al.*, 1999). We partition rays into multiple linear segments, with which we calculate the angle between the propagation direction and the Earth's rotation axis. We apply equation (3) to compute the polarization for each linear ray segment, which is then multiplied by the segment's corresponding travel-time duration to find the segment's polarization anomaly. All polarization anomalies from each segment are summed to find the total polarization anomaly. The corresponding code is available in Data and Resources.

Figure 6a illustrates the calculation of the Coriolis force from equation (3) of *PKS* for the southern explosion. *PKS* has nearly vertical incidence angle, for which we only need to consider the *S* phase from the CMB to the receiver, along with the *PKS* triplication. In Figure 6b, we apply the same technique to each *S* leg of *SKS*—one beneath the source and the other beneath the receiver. Figure 6b,c illustrates that Earth's rotation only impacts the polarization measurement of the shear wave from the CMB to the receiver. The measured polarizations are nearly identical to the calculations for the receiver side *S* leg of SKS, not the sum of the calculations of both *S* legs (one beneath the source and the receiver). Because of the *SV-P* conversion at the CMB beneath the source, all rotation of the shear wave before *SKS* that enters the core is removed at the CMB.

Wavefronts and the Coriolis force

We showed in the previous sections that *S*-wave polarizations are affected by the Coriolis force by varying amounts depending on the ray direction and propagation time (from 2° to 7°). We next address whether the wavefronts are sensitive to the Coriolis force. This analysis extends the observations of Sens-Schönfelder *et al.* (2015), who show observations with USArray that wavefronts are not affected by Earth's rotation. We use synthetic seismograms of the USArray stations to

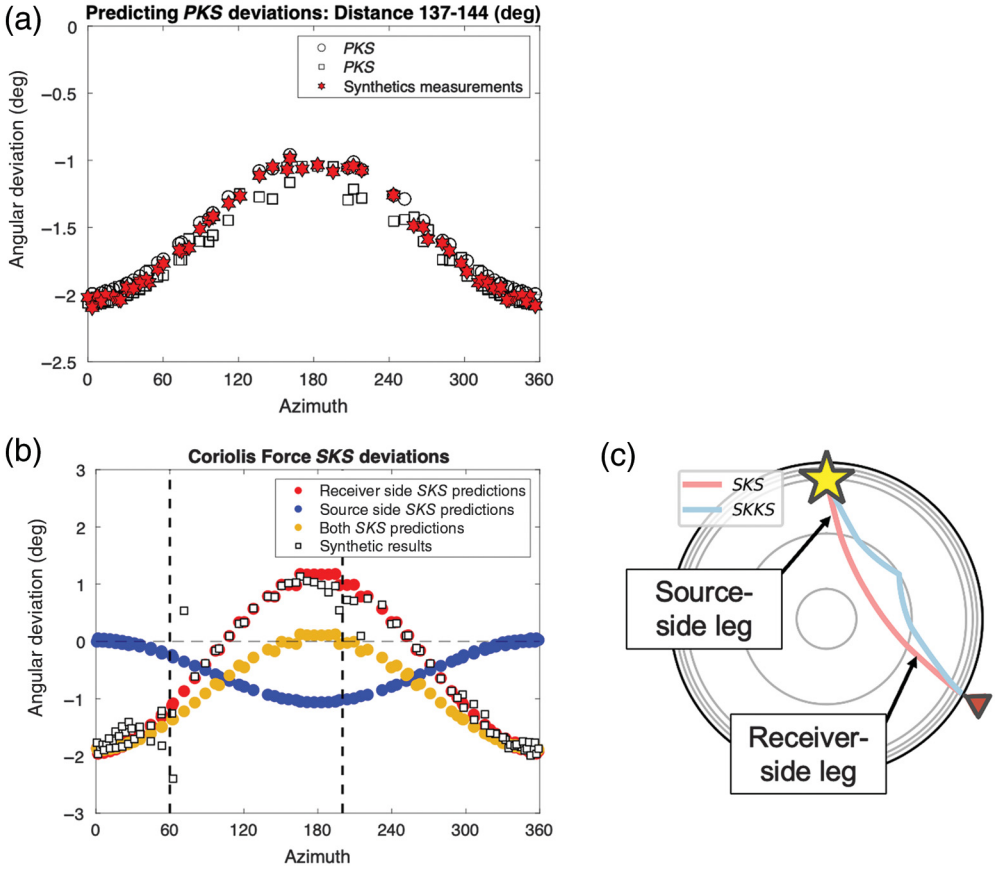

Figure 6. (a) *PKS* polarization (°) measurements (red stars) from southern explosion (*PKS*: 137°–144° distance) as compared to equation (2) (black circles). (b) Selected *SKS* polarization (°) measurements (red squares) and predictions based on equation (2) for *S* leg of *SKS* from core–mantle boundary (CMB) to receiver (blue circles), the *S* leg from source to the CMB (orange circles), and both *S* legs (yellow circles) for 110°–120° distance. A MATLAB routine is provided in the supplemental material to reproduce this figure. (c) Ray paths of *SKS* and *SKKS*, identifying the source-side shear-wave leg and the receiver-side shear-wave leg. *SKS* is a compressional wave in the outer core.

capture back azimuthal projections from 226 two additional earthquakes (see Table S4). These earthquakes are ideal, because they have high amplitudes at the azimuths recorded on the USArray. Back-azimuthal projections are important in the interpretation of waves that are subjected to scattering (e.g., Kaneshima and Helffrich, 1998) or out-of-plane reflections (e.g., Pisconti *et al.*, 2019). Polarization anomalies are often interpreted as a ray propagating out-of-plane; therefore, back azimuthal projections are a confirmation tool to specifically identify the ray's true back azimuth.

We apply a vespagram process on the synthetic seismograms to measure slowness and the direction of wave propagation (back azimuth) to selected subarrays of the USArray that demonstrate strong polarization deviations due to the Coriolis force of 3°–4.5° and 0.5°–1.5° for *S* and *SKS* waves, respectively (Fig. S2). We construct two subarrays, each consisting of 15 stations, located around a central point, following the method of Frost *et al.* (2020). Using the radial-component seismograms, we window the traces 35 s prior to and after the expected arrival times for PREM (Dziewonski and Anderson, 1981). We simultaneously grid search over slownesses from 0 to 9 s/deg in 0.1 s/deg increments and back azimuths of ±20° in 1° increments relative to the great-circle path and construct vespagrams (Davies *et al.*, 1971). We select the best-fitting slowness and back azimuth from the maximum beam amplitude. Residual back azimuths are measured relative to the great-circle path; travel time and slowness anomalies are measured relative to expectations from PREM calculated at the central point of the array.

Overall, we find no difference in the back azimuth or slowness between those calculated with rotating and nonrotating seismograms (Fig. 7). Earth's Coriolis force causes a rotation of the particle motion out of the expected plane of polarization but produces no change in the propagation of the wavefront.

Crustal and mantle heterogeneity

We calculate the same events from the Realistic earthquake sources section for GLAD-M15. In general, the polarization anomalies increase as more heterogeneity is included (see Fig. 8 and Fig. S3) for all distances and azimuths. To evaluate if crustal heterogeneity contributes to polarization anomalies, we also calculate the *SKS* polarizations of three events close to each other in location for PREM and two 3D models: S40RTS with a 1D averaged crust and S40RTS with a 3D crust. We calculate the root mean squared error (rmse) of the polarization anomalies between PREM and the 3D models. The mantle is the main source of the heterogeneities observed in polarization anomalies, making up 81% of the total rmse value; however, the crust is responsible for 19% of the RMS. Figure S4 illustrates that a 3D crust only adds a modest effect on the polarization anomalies. In general, mantle heterogeneity dominates polarization deviations of *SKS* compared to the effect of the Coriolis force.

Finally, we compare two events (one deep and one shallow) between two different 3D models: GLAD-M15 and GLAD-M25 (Fig. S5). The latter model produces increased polarization anomalies for these two events compared to GLAD-M15

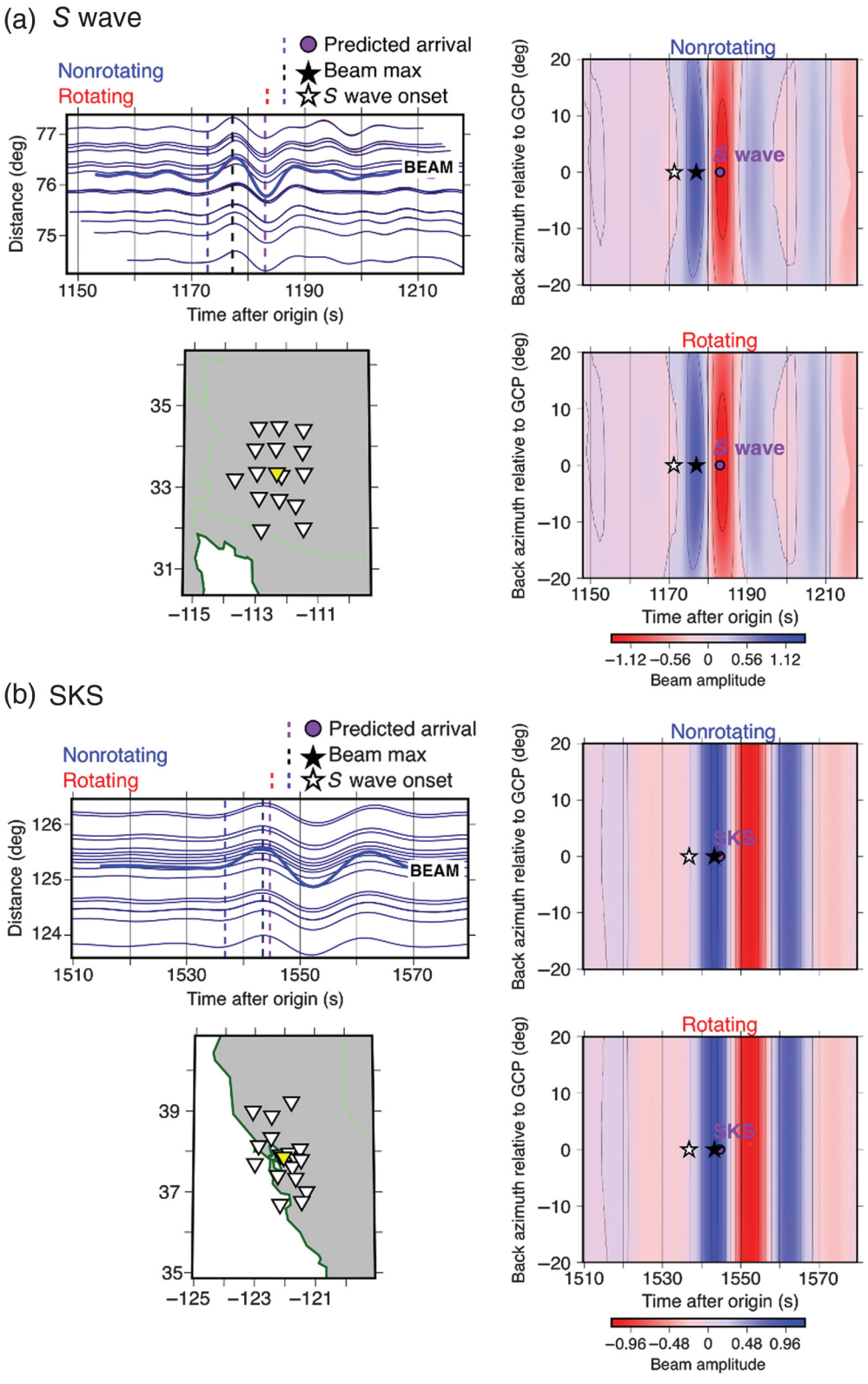

Figure 7. Back-azimuth vespagrams of synthetics for an (a) *S* wave and (b) *SKS* wave. Beams (solid blue [nonrotating Earth] and red [rotating Earth] lines) are constructed by varying the back azimuth with a fixed slowness. Waveforms are plotted with thinner blue and red lines with time after the origin (seconds) versus distance from the source (degrees) for a subarray (white triangles) from the USArray with the central point of the array (average station location) in yellow. Back-azimuth beam stacks (displayed as beam amplitude) for the nonrotating and rotating synthetics are plotted, showing the predicted arrival based on PREM (purple lines and dots), the maximum of the beam amplitude (black lines and stars), and the *S*-wave onset (blue lines and white stars).

by 0.25°(2σ) for *SKS* and *SKKS*. GLAD-M25 has increased resolution and features in the mantle up to spherical harmonic degree of 60 (Lei *et al.*, 2020) with larger seismic wavespeed perturbations. We observe that polarization anomalies from the calculated polarization becomes larger due to lateral variations in the mantle and crust as resolution increases.

DISCUSSION

Traditionally, *SKS* is expected to always be polarized along the great-circle back azimuth (e.g., Silver, 1996; Hall *et al.*, 2004; Restivo and Helffrich, 2006); however, Earth's rotation and crustal and mantle structure can introduce *SKS* polarization anomalies, based on this study. Restivo and Helffrich (2006) hypothesized that the sources of *SK(K)S* polarization anomalies could be dipping discontinuities within the D" layer or CMB topography based on numerical modeling of wave propagation in a homogeneous, nonrotating Earth. Walpole *et al.* (2014) expanded the dataset of *SKS* polarizations and noted a smaller scatter in *SKS* polarizations than Restivo and Helffrich (2006), as Walpole *et al.* (2014) had much stricter quality control cutoffs (Fig. 9). Therefore, accurate polarization anomalies are needed to constrain potential dipping layers or topography. Without correcting for long-wavelength seismic heterogeneities and the Coriolis force, the observed *SK(K)S* polarizations from Restivo and Helffrich (2006) would require the CMB topography to be greater than 50 km

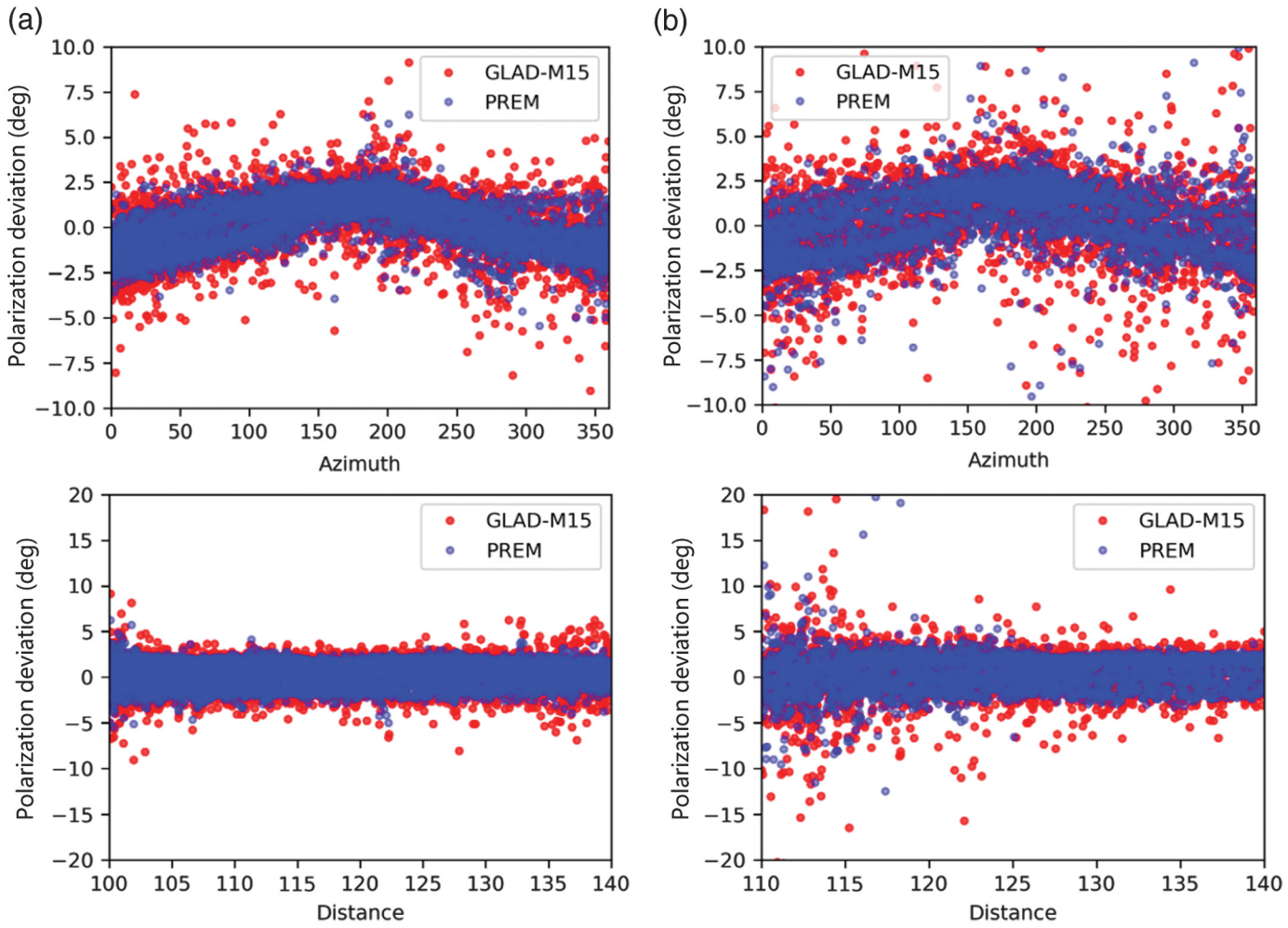

Figure 8. Polarization measurements relative to the azimuth (angular deviation, in degrees) and arc distance (°) from all earthquakes for selected phases: (a) *SKS* (100°–140° arc distance) and (b) *SKKS* (110°–140° arc distance). All nodal planes have been removed. PREM is represented as blue dots. GLAD-M15 is represented as red dots.

over a lateral distance of 500 km, much larger than the previously suggested values of 1.5–6 km (e.g., Morelli and Dziewonski, 1987; Sze and van der Hilst, 2003).

Figure 9 illustrates the distribution of polarization measurements of all 21 events for *SKS* and *SKKS* for PREM and GLAD-M15 from this study and polarizations documented in Restivo and Helffrich (2006) and Walpole *et al.* (2014), who also measured *SKS* and *SKKS* SWS. We discard all records with azimuths from the source that are near the nodal plane of each earthquake. For *SKS* and *SKKS*, we use 100°–140° and 110°–140° distance ranges, respectively, to avoid any complications of *S* and S_{diff} phases and to be consistent with Walpole *et al.* (2014). Restivo and Helffrich (2006) found standard deviations of 16.36°(2σ) and 21.76°(2σ) for hundreds of *SK(K)S* polarizations, respectively. Walpole *et al.* (2014) found a smaller *SKS* polarization standard deviation of 10.6°(2σ) with ~15,000 polarizations (see Fig. 9). Figure S6 shows the same polarization measurements in azimuth from the event and distance. *SKS* and *SKKS* polarizations deviate from the back azimuth up to 2.8°(2σ) and 3.4°(2σ) for PREM and up to 4.0°(2σ) and 5.8°(2σ) for GLAD-M15, respectively. We find that 3D mantle heterogeneities do increase the scatter of polarization anomalies (Table S3, Fig. 8). The mean difference in polarization anomalies between these two models is nearly 0° with standard deviations of 2.0°(2σ) for SKS and 4.4°(2σ) for SKKS.

The azimuthal distribution of these earthquakes and arc distances from each study are different. The earthquake and receiver location and arc distance do influence the overall polarization anomaly. The maximum polarization anomaly will be for rays that propagate along Earth's rotation axis. For these reasons, we used realistic earthquakes with an even global distribution. In addition, there is a bias in the study of Walpole *et al.* (2014), because most of the observations are made at the USArray stations, where many of the same observations are made at multiple stations, spatially near each other. As a result, the mean of the polarization anomalies is shifted away from zero, because most of the dataset is measured in the Northern Hemisphere (Table S3, Fig. 9c: black curve). We have calculated the expected polarization changes of this dataset due

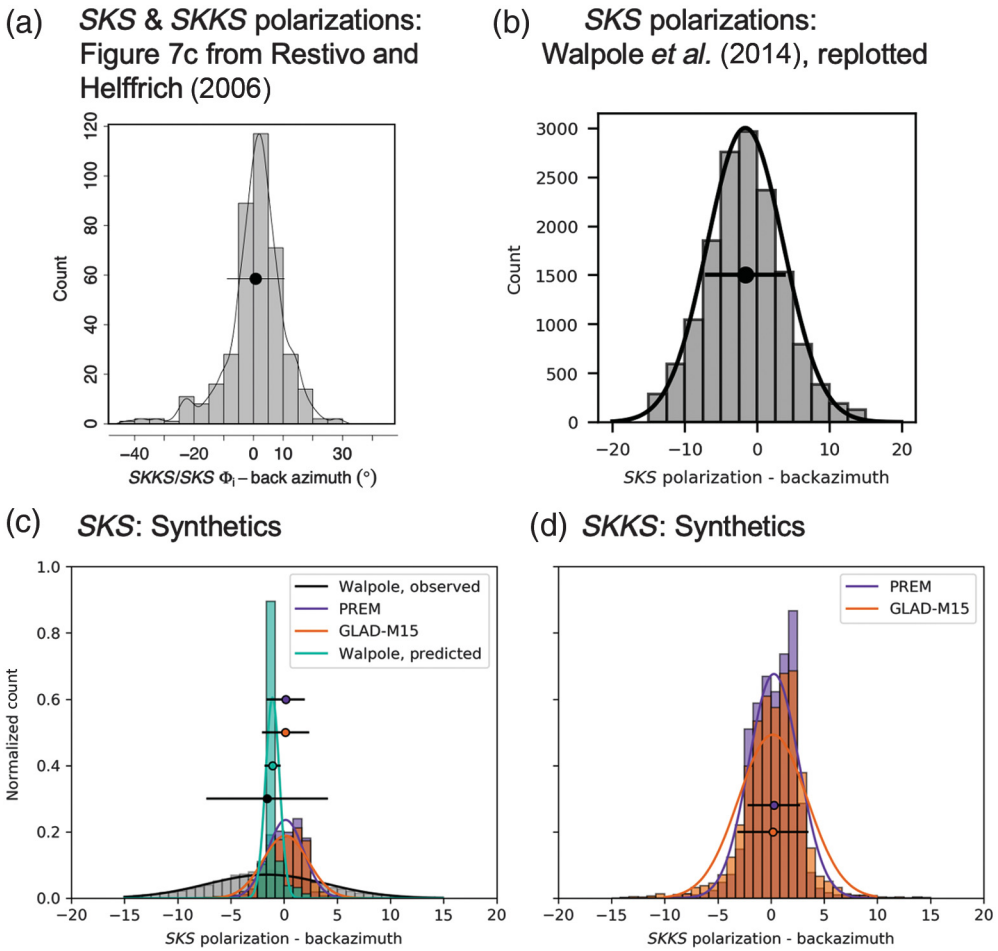

Figure 9. (a) Polarization measurements of *SK(K)S* (Fig. 7c reprinted with permission from Oxford University Press from Restivo and Helffrich, 2006) relative to the back azimuth. Mean of observations (black dot) and one standard deviation (black bar) are plotted. (b) *SKS* polarization measurements relative to the back azimuth, replotted from Walpole *et al.* (2014). Selected polarizations are from null and split measurements only. (c) Histogram of *SKS* polarizations measured from synthetics for 21 earthquakes for distances 100°–140° (PREM: blue; GLAD-M15: red). In addition, the histogram from panel (b) is plotted in black. The predicted *SKS* polarization based on earthquake locations (green dots in Fig. 1) is plotted in teal. Mean of observations (dots) and one standard deviation (black bars) are plotted. (d) Same as panel (c) but *SKKS* for distances 110°–140°. Note that the *x* axis is different in panel (a).

to the Coriolis force for each event and station pair with 1D ray tracing (see Fig. 9: blue curve). The same bias (a shift in the mean away from zero) we observe in the Walpole dataset is also present in our calculated polarization anomalies, which illustrates that the Coriolis force is impacting the polarization anomalies. Finally, we do show that there is a weak cosine relationship in all polarizations of the Walpole dataset, indicating the influence of the Coriolis force (Fig. S6).

Consequently, nearly one-third of all *SKS* polarizations in Walpole *et al.* (2014) can be explained by 3D mantle heterogeneities (based on GLAD-M15 simulations) and the Coriolis force. The remaining polarization anomalies beyond ±3.4° are likely due to a combination of small-scale heterogeneities, dipping layer, and/or topography. Therefore, it may be worthwhile to revisit estimates of the CMB topography using *SKS* and *SKKS* polarizations by taking 3D mantle structure and the Coriolis force into account.

To interrogate Earth structure with *SK(K)S* polarizations, one can subtract the influence of the Coriolis force from shear-wave polarizations using ray tracing (1D or 3D) and equation (2). The 3D ray tracing considers ray bending due to 3D effects, which is negligible relative to the Coriolis force and highly dependent on the Earth model. When the polarization anomalies are subtracted from the nonrotating Earth, the residual polarization anomalies for GLAD-M15 match those for PREM. Figure S7 compares polarization anomalies of *PKS* for PREM and GLAD-M15 for a rotating and nonrotating Earth, illustrating the scatter that can be introduced into polarization anomalies by 3D Earth structure. Therefore, 1D ray tracing is adequate to calculate the influence of the Coriolis force for well-isolated phases.

Heterogeneous structure can significantly impact the arrival times of *S*, S_{diff}, *SKS*, and *SKKS*, for which these shear waves can introduce errors into polarization measurements. Other *P* or *S* waves that introduce radial or transverse component energy can slightly deviate the calculated polarizations as well (Fig. S8). Therefore, numerical modeling of wave propagation can be useful in eliminating all possible sources of polarization anomalies (superimposed phases, the Coriolis force, source effects, and long wavelength heterogeneity) before attributing the total polarization anomaly to topography, velocity gradients, and/or dipping interfaces. In our synthetics, at longer periods, there is some frequency dependence observed (likely due to phases overlapping each other in the measurement time window); therefore, synthetic seismograms should be produced at the appropriate frequency range (Snieder *et al.*, 2016; Fig. S9).

The influence of the Coriolis force on SWS and other measurements

Because of the Coriolis force, the polarization of shear waves is rotated. Because that rotation is the same for the two *S*-wave components (e.g., *SH* and *SV*), ellipticity caused by seismic anisotropy is not affected by Earth's rotation other than an overall rotation of the ellipsoidal particle motion. The Coriolis force may have a small influence on SWS depending on the measurement technique, because the impacted shear waves (e.g., *SKS*) are now misaligned with the great-circle back azimuth. Tian *et al.* (2011) explored the effects of misaligned *SKS* and *SKKS* phases on SWS measurements, and found that small misalignments can introduce small errors when using any technique to measure SWS. However, larger errors may occur when using techniques that rely on *SKS* polarizations to be aligned with the radial component (Silver and Chan, 1991; Chevrot, 2000; Monteiller and Chevrot, 2010). Expected polarization anomalies of *SK(K)S* (<5°) may cause significant errors in SWS measurements when using the linear minimization method, as shown by Tian *et al.* (2011). Therefore, consideration of polarization anomalies due to the Coriolis force is needed when applying the transverse component minimization technique, such as applying a rotation to the seismograms where transverse component energy is at a minimum. To confirm that the Coriolis force does not affect the seismic anisotropy measurements, we measure the SWS intensity (Chevrot, 2000) and cross-correlation delay times (Ando, 1984) for all the 21 events in this study for PREM (see section 8 in the supplement and Fig. 10). There is no introduction of apparent anisotropy for any *SKS*, *SKKS*, or *PKS* phase, and the introduced errors due to the Coriolis force and long-wavelength structure from GLAD-M15 are small (<0.2 s). Except at short-arc distances, there is apparent anisotropy because of the interference of *S* and S_{diff} (Tono and Fukao, 2013).

Mantle shear phases, *S*, *ScS*, and *PcS*, are also used for SWS (Wookey *et al.*, 2005; He and Long, 2011; Walpole *et al.*, 2017). The incoming polarization of a mantle shear wave will control the resulting apparent seismic anisotropy measured at the station because of how the wave is polarized when interacting with an anisotropic medium. In addition, upper mantle corrections (Wookey *et al.*, 2005; Creasy *et al.*, 2017) are used to correct an *S* or *ScS* wave to estimate anisotropy in the D" layer or the upper mantle beneath the source. The polarization changes could result in complications of modeling shear-wave anisotropy and correcting for upper mantle anisotropy (up to 10° or more for certain azimuths). The effect of Earth's rotation on mantle SWS measurements with an anisotropic Earth model is worthy of the future research, because mantle shear waves are more impacted than core phases by the Coriolis force.

Polarization anomalies of body waves may have other implications other than SWS. Studies that use polarizations, such as station misalignment, should consider the Coriolis force (Reiss and Rümpker, 2017; Vidale, 1986; Eakin *et al.*, 2018; Park and Ishii, 2018). Traditionally, *SKS* polarization anomalies relative to the great-circle back azimuth at a single station are analyzed so as to center the mean of all polarization anomalies to zero for correcting a misaligned seismic station (e.g., Reiss and Rümpker, 2017; Eakin *et al.*, 2018). Based on synthetic seismograms of earthquakes, the polarization anomalies of *SKS* and *SKKS* can have nonzero means (see Table S3), even though we explore the entire azimuthal range of earthquake propagation and consider an even earthquake distribution. Sampling only certain earthquake azimuths (i.e., only earthquakes from a certain region) may shift the mean from 0°, making station misalignment methods not as accurate. *P* waves may be more suitable to use for station alignment than *S* waves if ignoring the Coriolis force and the impact of superimposed phases, because direct *P* waves are not significantly affected by the Earth's rotation. Other impacts of the Coriolis force on polarization studies could be the determination of source mechanisms and *S*-to-*P* receiver functions, for which knowledge of the initial *S*-wave polarization is important. The polarization of the incoming *S* wave for receiver functions could change the resulting impedance contrast (e.g., Chen *et al.*, 2021).

CONCLUSION

The Earth's Coriolis force and 3D mantle heterogeneities introduce a measurable deviation of core phase polarizations from the great-circle back azimuth, resulting in polarization deviations up to ±3.4°(2σ) for *SKS*, for which measured polarizations of *SKS* can vary up to 10°–20° (2σ). Mantle shear waves are more impacted by Earth's rotation due to their longer propagation times, because core phases only retain Coriolis forces from the CMB to the receiver. Other nonstructure features can introduce additional polarization anomalies, such as other shear phases arriving within the same time window as the phase of interest, source effects (Fig. 5), and Earth's ellipticity (Fig. S11). As a result, Earth's rotation causes the *SH* and *SV* components to rotate away from the expected polarization (which can be calculated from the source mechanism or *P-SV* conversions at interfaces) and does not introduce any changes in the direction of wave propagation or significant impacts on SWS of core phases. However, studies that rely on *S*-wave polarizations, such as CMB topography, determination of source mechanisms, receiver functions, and station misalignment techniques, should take Earth's rotation into account. As a result, interpretations of shear-wave polarizations may overestimate the influence of heterogeneous structure if not taking the Coriolis force into account. It is straight forward to calculate the Coriolis force using 1D ray tracing and applying equation (3) to the shear-wave components of the phase of interest, because we have supplied a MATLAB (www.mathworks.com/products/matlab, last accessed January 2020) routine. Full-waveform simulations with a

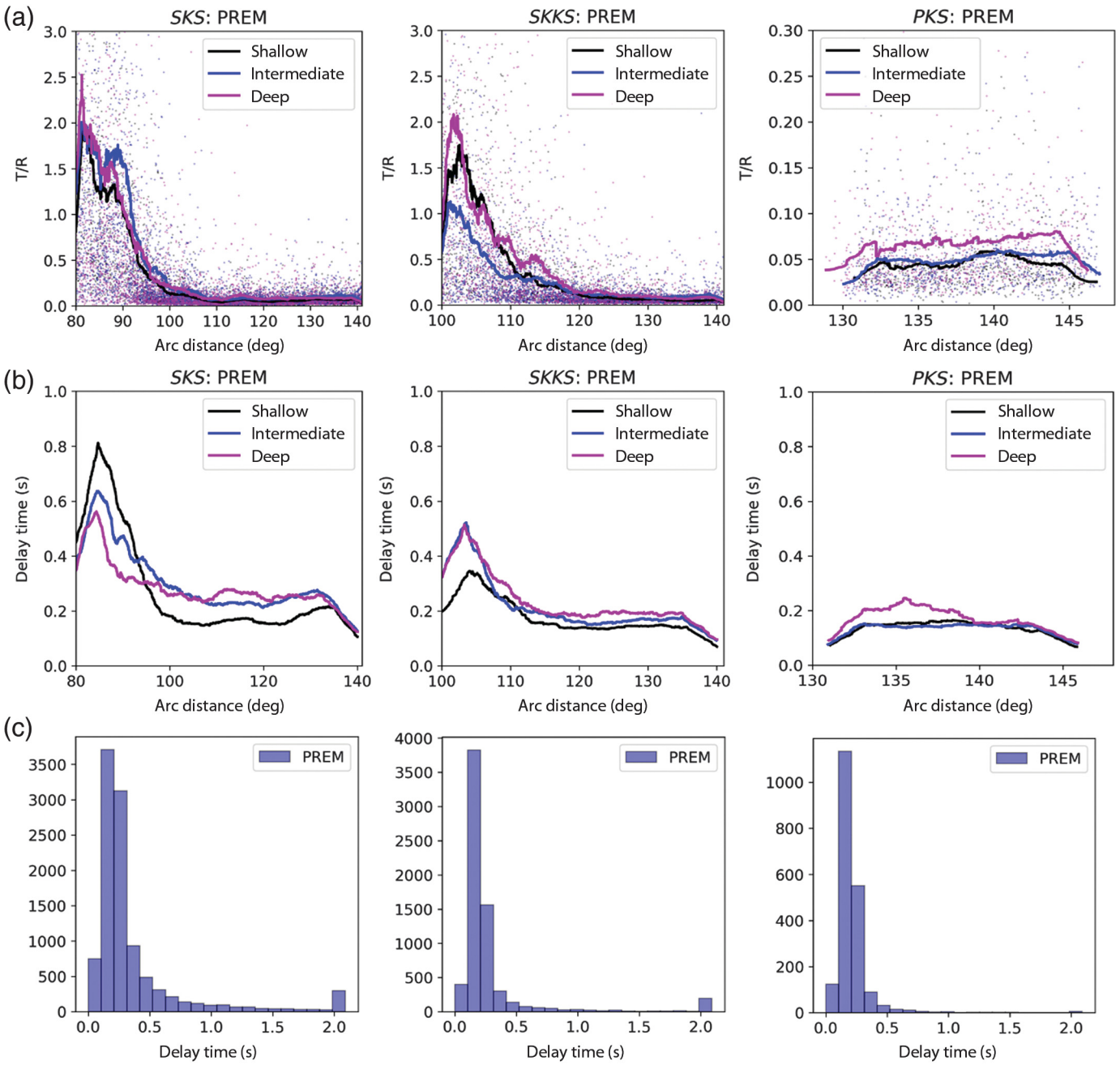

rotating Earth or normal mode calculations are another approach because all complications would be considered (e.g., source effects). Overall, shear-wave polarizations have significant potential in constraining scattering and CMB topography; therefore, nonstructural effects on polarization need to be considered before interpreting polarizations.

Figure 10. (a) The ratio of transverse over radial energy in the measurement window of an *SKS*, *SKKS*, or *PKS* wave for the PREM Earth model with a rotating Earth, shown as T/R over arc distance. The T/R value should be low for null splitting as these phases should be dominated by radial energy. Dots represent individual seismograms for which lines represent a moving average, which are also colored by the depth of the earthquake (shallow = 0–60 km, intermediate = 60–300 km, deep = 300–600 km). (b) Moving averages for measured delay times (second) from the seismograms over the same measurement window. (c) Histograms of delay times for each phase, which show the same data as displayed in the panel (b).

DATA AND RESOURCES

All information is provided to reproduce SPECFEM3D GLOBE simulations. We used earthquake sources from this the Global Centroid Moment Tensor (Global CMT) catalog (Ekström *et al.*, 2012). The supplemental material is available in a Mendeley data repository (Creasy, Neala [2023], "SKS Polarization Anomalies due to the Coriolis Force," Mendeley Data, V3, doi: 10.17632/kgh3ybvb88.3). Example parameter files are included to reproduce the SPECFEM3D GLOBE simulations in the supplemental material. Code to calculate Coriolis force polarization effect with 1D ray tracing is included in the supplemental material to reproduce Figure 6b in the main article.

DECLARATION OF COMPETING INTERESTS

The authors acknowledge that there are no conflicts of interest recorded.

ACKNOWLEDGMENTS

This work used the Extreme Science and Engineering Discovery Environment (XSEDE) Texas Advanced Computing Center (TACC) at The University of Texas at Austin and Expanse at UC San Diego through allocation TG-EES200011 using XSEDE resources (Towns *et al.*, 2014). The data were synthesized via the open-sourced SPECFEM3D GLOBE from CIG (https://geodynamics.org/resources/specfem3d, last accessed January 2020). This material is based upon work supported by the National Science Foundation under Award Number EAR-2027181 to Daniel A. Frost, EAR-1855206 to Neala Creasy, and EAR-2026931 to Ebru Bozdağ. The authors thank contributions and feedback from Ed Garnero, Maureen Long, Jonathan Wolf, and Adeolu Aderoju. The authors thank Reynaldo Vite Sanchez, Quancheng Huang, and Rachel Willis for testing MATLAB routines. The authors thank the contributions of two anonymous reviewers. The Los Alamos National Laboratory (LANL) access is available through LA-UR 23-22919.

REFERENCES

Ando, M. (1984). ScS polarization anisotropy around the Pacific Ocean, *J. Phys. Earth* **32,** no. 3, 179–195.

Backus, G., and F. Gilbert (1961). The rotational splitting of the free oscillations of the earth, *Proc. Natl. Acad. Sci. Unit. States Am.* **47,** no. 3, 362.

Bozdağ, E., and J. Trampert (2008). On crustal corrections in surface wave tomography, *Geophys. J. Int.* **172,** no. 3, 1066–1082.

Bozdağ, E., D. Peter, M. Lefebvre, D. Komatitsch, J. Tromp, J. Hill, N. Podhorszki, and D. Pugmire (2016). Global adjoint tomography: First-generation model, *Geophys. J. Int.* **207,** no. 3, 1739–1766.

Chen, X., J. Park, and V. Levin (2021). Anisotropic layering and seismic body waves: Deformation gradients, initial S-polarizations, and converted-wave birefringence, *Pure Appl. Geophys.* 1–23.

Chevrot, S. (2000). Multichannel analysis of shear wave splitting, *J. Geophys. Res.* **105,** no. B9, 21,579–21,590.

Creasy, N., M. D. Long, and H. A. Ford (2017). Deformation in the lowermost mantle beneath Australia from observations and models of seismic anisotropy, *J. Geophys. Res.* **122,** no. 7, 5243–5267.

Crotwell, H. P., T. J. Owens, and J. Ritsema (1999). The TauP toolkit: Flexible seismic travel-time and ray-path utilities, *Seismol. Res. Lett.* **70,** no. 2, 154–160.

Dahlen, F. A., and J. Tromp (1998). *Theoretical Global Seismology*, Princeton University Press, Princeton, New Jersey.

Davies, D., E. J. Kelly, and J. R. Filson (1971). Vespa process for analysis of seismic signals, *Nat. Phys. Sci.* **232,** 8–13, doi: 10.1038/physci232008a0

Dziewonski, A. M., and D. L. Anderson (1981). Preliminary reference earth model, *Phys. Earth Planet. In.* **25,** no. 4, 297–356.

Eakin, C. M., C. A. Rychert, and N. Harmon (2018). The role of oceanic transform faults in seafloor spreading: A global perspective from seismic anisotropy, *J. Geophys. Res.* **123,** no. 2, 1736–1751.

Ekström, G., M. Nettles, and A. Dziewonski (2012). The global CMT project 2004-2010: Centroid-moment tensors for 13,017 earthquakes, *Phys. Earth Planet. In.* **200,** 1–9.

Ferreira, A., J. Woodhouse, K. Visser, and J. Trampert (2010). On the robustness of global radially anisotropic surface wave tomography, *J. Geophys. Res.* **115,** no. B4, doi: 10.1029/2009JB006716.

Frost, D. A., B. Romanowicz, and S. Roecker (2020). Upper mantle slab under Alaska: Contribution to anomalous core-phase observations on south-Sandwich to Alaska paths, *Phys. Earth Planet. In.* **299,** doi: 10.1016/j.pepi.2020.106427

Hall, S. A., J. M. Kendall, and M. van der Baan (2004). Some comments on the effects of lower-mantle anisotropy on SKS and SKKS phases, *Phys. Earth Planet. In.* **146,** nos. 3/4, 469–481.

He, X., and M. D. Long (2011). Lowermost mantle anisotropy beneath the northwestern pacific: Evidence from PcS, ScS, SKS, and SKKS phases, *Geochem. Geophys. Geosys.* **12,** no. 12, doi: 10.1029/2011GC003779.

Kaneshima, S., and G. Helffrich (1998). Detection of lower mantle scatterers northeast of the Marianna subduction zone using short-period array data, *J. Geophys. Res.* **103,** no. B3, 4825–4838.

Komatitsch, D., and J. Tromp (2002a). Spectral-element simulations of global seismic wave propagation—ii. Three-dimensional models, oceans, rotation and self-gravitation, *Geophys. J. Int.* **150,** no. 1, 303–318.

Komatitsch, D., and J. Tromp (2002b). Spectral-element simulations of global seismic wave propagation—I. Validation, *Geophys. J. Int.* **149,** no. 2, 390–412.

Lei, W., Y. Ruan, E. Bozdağ, D. Peter, M. Lefebvre, D. Komatitsch, J. Tromp, J. Hill, N. Podhorszki, and D. Pugmire (2020). Global adjoint tomography—Model GLAD-m25, *Geophys. J. Int.* **223,** no. 1, 1–21.

Lekic, V., M. Panning, and B. Romanowicz (2010). A simple method for improving crustal corrections in waveform tomography, *Geophys. J. Int.* **182,** no. 1, 265–278.

Monteiller, V., and S. Chevrot (2010). How to make robust splitting measurements for single-station analysis and three-dimensional imaging of seismic anisotropy, *Geophys. J. Int.* **182,** no. 1, 311–328.

Morelli, A., and A. M. Dziewonski (1987). Topography of the core–mantle boundary and lateral homogeneity of the liquid core, *Nature* **325,** no. 6106, 678–683.

Park, J., and F. Gilbert (1986). Coupled free oscillations of an aspherical, dissipative, rotating earth: Galerkin theory, *J. Geophys. Res.* **91,** no. B7, 7241–7260.

Park, S., and M. Ishii (2018). Near-surface compressional and shear wave speeds constrained by body-wave polarization analysis, *Geophys. J. Int.* **213,** no. 3, 1559–1571.

Pisconti, A., C. Thomas, and J. Wookey (2019). Discriminating between causes of D" anisotropy using reflections and splitting measurements for a single path, *J. Geophys. Res.* **124,** no. 5, 4811–4830.

Reiss, M. C., and G. Rümpker (2017). Splitracer: MATLAB code and GUI for semiautomated analysis and interpretation of teleseismic shear-wave splitting, *Seismol. Res. Lett.* **88,** no. 2A, 392–409.

Restivo, A., and G. Helffrich (2006). Core—Mantle boundary structure investigated using SKS and SKKS polarization anomalies, *Geophys. J. Int.* **165,** no. 1, 288–302.

Ritsema, J., H. Van Heijst, J. Woodhouse, and A. Deuss (2009). Long-period body wave traveltimes through the crust: Implication for crustal corrections and seismic tomography, *Geophys. J. Int.* **179,** no. 2, 1255–1261.

Savage, M. (1999). Seismic anisotropy and mantle deformation: What have we learned from shear wave splitting? *Rev. Geophys.* **37,** no. 1, 65–106.

Schoenberg, M., and D. Censor (1973). Elastic waves in rotating media, *Q. Appl. Math.* **31,** no. 1, 115–125.

Sens-Schönfelder, C., R. Snieder, and S. Stahler (2015). The lack of equipartitioning in global body wave coda, *Geophys. Res. Lett.* **42,** 7483–7489.

Silver, P. G. (1996). Seismic anisotropy beneath the continents: Probing the depths of geology, *Annu. Rev. Earth Planet. Sci.* **24,** no. 1, 385–432.

Silver, P. G., and W. W. Chan (1991). Shear wave splitting and subcontinental mantle deformation, *J. Geophys. Res.* **96,** no. B10, 16,429–16,454.

Snieder, R., and C. Sens-Schönfelder (2021). Local coupling and conversion of surface waves due to earth's rotation. part 1: Theory, *Geophys. J. Int.* **225,** no. 1, 158–175.

Snieder, R., C. Sens-Schönfelder, E. Ruigrok, and K. Shiomi (2016). Seismic shear waves as Foucault pendulum, *Geophys. Res. Lett.* **43,** no. 6, 2576–2581.

Sze, E. K., and R. D. van der Hilst (2003). Core mantle boundary topography from short period pcp, pkp, and pkkp data, *Phys. Earth Planet. In.* **135,** no. 1, 27–46.

Tian, X., J. Zhang, S. Si, J. Wang, Y. Chen, and Z. Zhang (2011). SKS splitting measurements with horizontal component misalignment, *Geophys. J. Int.* **185,** no. 1, 329–340.

Tono, Y., and Y. Fukao (2013). Shear-wave splitting apparently caused by contamination of P-to-S or S-to-P converted waves, *Bull. Seismol. Soc. Am.* **103,** no. 2A, 950–957.

Towns, J., T. Cockerill, M. Dahan, I. Foster, K. Gaither, A. Grimshaw, V. Hazlewood, S. Lathrop, D. Lifka, G. D. Peterson, *et al.* (2014). XSEDE: Accelerating scientific discovery, *Comput. Sci. Eng.* **16,** no. 5, 62–74.

Tromp, J. (1994). Surface-wave propagation on a rotating, anisotropic earth, *Geophys. J. Int.* **117,** no. 1, 141–152.

Vidale, J. E. (1986). Complex polarization analysis of particle motion, *Bull. Seismol. Soc. Am.* **76,** no. 5, 1393–1405.

Walpole, J., J. Wookey, J. M. Kendall, and T. G. Masters (2017). Seismic anisotropy and mantle flow below subducting slabs, *Earth Planet. Sci. Lett.* **465,** 155–167.

Walpole, J., J. Wookey, G. Masters, and J. Kendall (2014). A uniformly processed data set of SKS shear wave splitting measurements: A global investigation of upper mantle anisotropy beneath seismic stations, *Geochem. Geophys. Geosys.* **15,** no. 5, 1991–2010.

Wookey, J., J. M. Kendall, and G. Rümpker (2005). Lowermost mantle anisotropy beneath the north pacific from differential s—scs splitting, *Geophys. J. Int.* **161,** no. 3, 829–838.

Manuscript received 6 June 2023
Published online 3 October 2023